The estimated GSTs from all the boreholes are similar (Fig. 3). The record of the GSTs of the most recent hundred years agrees with the trend of the average surface air temperatures of the Northern Hemisphere (3) and that of central Ontario (16), the nearest region where century-long reliable meteorological data are available. All three holes show a cold period near the end of the 19th century, which is in agreement with tree-ring data from the United States and southwestern Canada (5). Tree-ring data from the high-latitude area of Canada and Alaska (17–19) also suggest such a cold period but with a temperature minimum about 50 years earlier. The two deeper holes, 022 and 024, show a less well resolved older cold period ~400 years ago, which agrees with what has been identified by historical and glacial studies as the Little Ice Age (20, 21). Because of the limitation imposed by borehole depths (shown on each curve) and the nature of heat diffusion, GST variations before A.D. 1500 cannot be resolved with confidence.

The land where the boreholes were drilled is low and flat in the south and higher and more rugged in the north, with an average difference in elevation of about 70 m. Boreholes 022 and 024 are located in the flat low area; therefore, the topographic effect on the geothermal gradient is negligible. Hole 389 is at a higher elevation and on a south-facing slope. Stronger solar radiation on the slope causes the upper part of the temperature profile to be "bent" toward the warm side, which results in a higher mean surface temperature and an apparent slight warming trend in the GST. Because the sites that were investigated are covered by snow in winter, the annual mean GST is higher than that of the surface air temperature.

The Lac Dufault paleotemperature results are considered the most reliable that are available because of the unmatched quality of the thermal data. We have also studied deep borehole data from another 19 sites in Canada. Although conditions are not as favorable at any of these sites as at Lac Dufault, GST estimates from most of them do show a cold period before the recent climatic warming. Five of the sites yield results nearly identical to those of Lac Dufault for the last 200 years. The GSTs from the two sites nearest Lac Dufault (Fig. 4) substantiate the Lac Dufault results, although their uncertainties are larger.

In order to determine whether the recent warming has been caused by human activities, we need to know whether the current temperature and the current rate of temperature increase are significantly above normal, that is, the average temperature and the average rate of temperature increase during the centuries or millennia before industrialization. Because of the decrease in the resolution of GST back in time, we cannot assess the rate of increase. However, the long-term mean GST can be estimated, and this can be compared with the current temperatures. The deeper the borehole, the better is the mean GST that is determined, but our test using a 3-km hole shows that this value is robust if the borehole is deeper than 600 m. By a comparison of temperatures only (Figs. 3 and 4), the recent warming has indeed resulted in a temperature that is 1° to 2°C higher than average, but the warming is partially a recovery from a cold period.

REFERENCES AND NOTES

1. P. D. Jones *et al.*, *J. Clim. Appl. Meteorol.* **25**, 1213 (1986).
2. H. W. Ellsaesser, M. C. MacCracken, J. J. Walton, S. L. Grotch, *Rev. Geophys.* **24**, 745 (1986).
3. J. Hansen and S. Lebedeff, *J. Geophys. Res.* **92**, 13345 (1987).
4. L. M. Libby, in *Climate History, Periodicity, and Predictability*, M. Rampino, J. Sanders, W. Newman, L. Konigsson, Eds. (Van Nostrand Reinhold, New York, 1987).
5. H. C. Fritts and J. M. Lough, *Clim. Change* **7**, 203 (1985).
6. E. Cook *et al.*, *Science* **253**, 1266 (1991).
7. A. E. Beck and A. Judge, *Geophys. J. R. Astron. Soc.* **18**, 145 (1969).
8. V. Cermak, *Palaeogeogr. Palaeoclimatol. Palaeoecol.* **10**, 1 (1971).
9. A. H. Lachenbruch and B. V. Marshall, *Science* **234**, 689 (1986).
10. S. B. Nielsen and A. E. Beck, *Tectonophysics* **164**, 345 (1989).
11. P. Y. Shen and A. E. Beck, *J. Geophys. Res.* **96**, 19965 (1991).
12. K. Wang, *ibid.* **97**, 2095 (1992).
13. H. Beltrami and J. C. Mareschal, *Geophys. Res. Lett.* **4**, 605 (1991).
14. T. J. Lewis and A. E. Beck, *Tectonophysics* **41**, 41 (1977).
15. A. Tarantola and B. Valette, *Rev. Geophys. Space Phys.* **20**, 219 (1982).
16. R. W. Longley, in *Proceedings of Toronto Meteorological Conference* (Royal Meteorological Society, London, 1953).
17. G. C. Jacoby and E. R. Cook, *Arct. Alp. Res.* **13**, 409 (1981).
18. ______, L. D. Ulan, *Quat. Res. (NY)* **23**, 18 (1985).
19. G. C. Jacoby and R. D'Arrigo, *Clim. Change* **14**, 39 (1989).
20. H. H. Lamb, *Climate: Present, Past and Future* (Methuen, London, 1977), vol. 2.
21. J. M. Grove, *The Little Ice Age* (Methuen, London, 1988).

22. K.W. holds a Canadian Government Laboratory Visiting Fellowship and is partially supported by the U.S. Geological Survey through an extramural contract. We thank D. S. Chapman, R. D. Hyndman, P. F. Hoffman, H. Beltrami, and an anonymous reviewer for valuable suggestions. Geological Survey of Canada contribution 48091.

6 January 1992; accepted 12 March 1992

Stress Diffusion Along the San Andreas Fault at Parkfield, California

P. E. Malin and M. G. Alvarez

Beginning in January 1990, the epicenters of microearthquakes associated with a 12-month increase in seismicity near Parkfield, California, moved northwest to southeast along the San Andreas fault. During this sequence of events, the locally variable rate of cumulative seismic moment increased. This increase implies a local increase in fault slip. These data suggest that a southeastwardly diffusing stress front propagated along the San Andreas fault at a speed of 30 to 50 kilometers per year. Evidently, this front did not load the Parkfield asperities fast enough to produce a moderate earthquake; however, a future front might do so.

Since mid-1987, the microearthquake activity of the San Andreas fault near Parkfield, California, has been monitored by the use of a ten-station network of borehole seismographs (Fig. 1, A and B). This region has the potential for moderate earthquakes at some time in the next few years (1–3). On the basis of magnitude-distance statistics, the distribution of earthquakes detected by the network is complete to roughly magnitude M = 0 near the center of the network and M = 0.25 overall (4). By the beginning of 1989, we had identified two seismically quiet patches of fault on which the future earthquakes might take place (4). The hypocentral locations of earthquakes observed since 1989 have not filled in the two aseismic patches we found then. Instead, they have begun to define clusters of intense activity, particularly north of the network.

Before 1990, the cumulative moments (effectively the sum of the fault areas times their slips) in the regions around the patches increased at roughly constant rates, with one exception, a large step in the cumulative moment produced by an M ~ 4 earthquake in May 1989, midway between Middle Mountain and Gold Hill. After the beginning of 1990, the cumulative moment rates in the Parkfield area began changing as a function of both time and location. Between January 1990 and May 1991, we observed a rapid increase in the cumulative moment

Department of Geology, Duke University, Durham, NC 27706

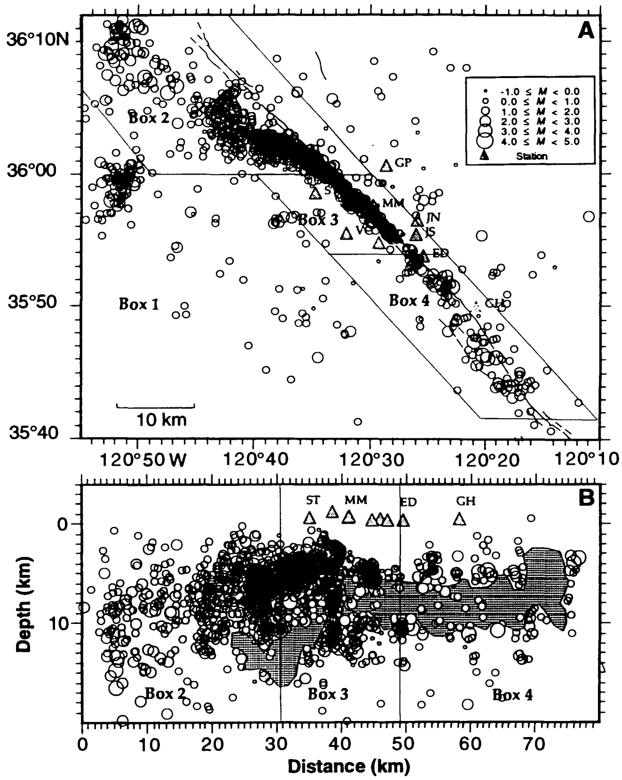

Fig. 1. A map (**A**) and an along-fault cross section (**B**) showing the trace of the Parkfield section of the San Andreas fault (*6*), locations of the borehole seismographs, the epicenters and hypocenters of 1952 microearthquakes detected between 1.1.1988 and 5.1.1991, and the regional boxes discussed in the text and subsequent figures. The westward fanning of events in box 2 is probably due to the lack of stations and to the faster seismic velocities in this region. Only events on the San Andreas fault have been projected onto the cross section. The two shaded regions indicate the approximate outlines of the aseismic patches where moderate earthquakes might take place in the future (*4*). Station MM is on Middle Mountain, station GH on Gold Hill, station ST on Stockdale Mountain, and station ED on Eades Ranch.

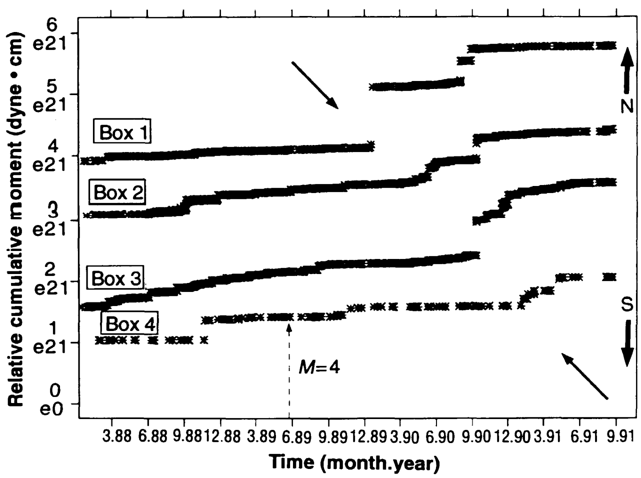

Fig. 2. The cumulative moments of Parkfield earthquakes by region, illustrating the southward migration of earthquake-related fault slip described in the text. The $M \sim 4$ event of 29 May 1989 was removed from the moment contribution at the time shown by the vertical dotted line. Arrows indicate the proposed stress diffusion front.

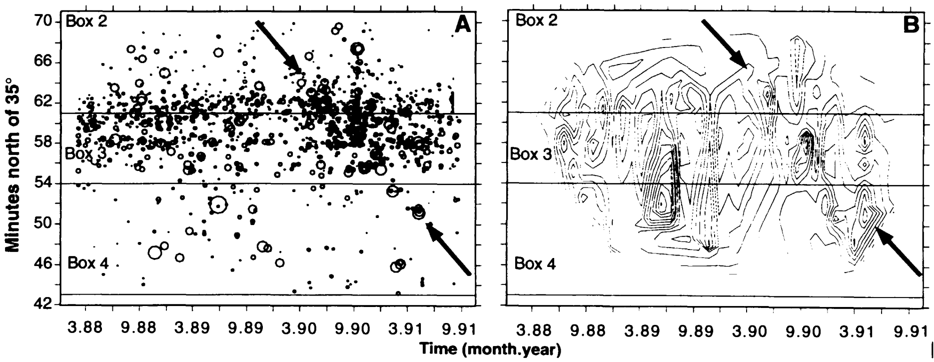

Fig. 3. (**A**) Earthquake magnitudes along the San Andreas fault as a function of latitude and time. (**B**) Magnitude-latitude-time plot after contouring. The magnitudes of the events are represented by circles of different sizes, with the May 1989 $M \sim 4$ earthquake being the largest and $M \sim 0$ the smallest (see Fig. 1, A and B). Arrows point out the proposed stress diffusion front.

around the seismically quiet patches, apparently beginning in the region northwest of Parkfield and moving progressively southeast along the San Andreas fault.

The cumulative moment of Parkfield earthquakes, between January 1988 and September 1991, increased discontinuously (Fig. 2) (*5*). To see the southeastwardly propagating rapid increase in cumulative moment, we grouped the cumulative moments into four regions, or "boxes" (Fig. 1A). Box 1 contains all the events that took place off the San Andreas fault, most of which are located to the north and west of the borehole seismograph network. Boxes 2, 3, and 4 divide the seismicity on the fault into northern, central, and southern segments, with box 3 containing the hypocenter of the 1966 Parkfield earthquake. It appears that the rapid increase in cumulative moment began in January 1990 in box 1. Subsequently, rapid increases in the cumulative moment began in box 2 in April 1990, in box 3 in September 1990, and in box 4 in January 1991. The $M \sim 4$ event of May 1989, which occurred in box 4, was omitted from this analysis because its moment was much larger than the full scale shown in Fig. 2 and its removal does not affect our conclusions.

Our conclusions about the southeastwardly moving episode of increased moment and implied slip are not sensitive to our choice of boxes because other arrangements of their boundaries give the same results. To show this, and to highlight the movement of increased moment on the San Andreas fault itself, we have plotted the earthquake magnitudes on the fault (boxes 2, 3, and 4) as a function of their latitudes and times of occurrence (Fig. 3A). To emphasize the characteristics of the increased slip episode, we have contoured this plot (Fig. 3B). The space-time distribution of magnitudes was smoothed so that a stable set of contours could be found.

Like the regionalized cumulative moments, the magnitude-latitude-time plots give an indication of earthquake-produced fault slip. On the contour plot, closely spaced contours imply rapid changes in slip. Before 1990, the slip rate at any given latitude was relatively constant, and the 29 May 1989 $M \sim 4$ earthquake dominated the magnitude-latitude-time topography. Beginning in 1990, a period of quiescence, which varied with latitude, took place and lasted only a matter of weeks in the north (36° and to the north) and on the order of a year in the south (35°54′ and to the south). In the contour plot, the onset of the earthquake sequence is indicated by closely spaced contours, which move to lower latitudes with increasing time. The episode of increased slip generally lasted a few months, after which the seismicity returned to its pre-1990 pattern.

In the present arrangement, box 3 corresponds to the segment of the San Andreas fault with the greatest spatial clustering of microearthquakes, whereas boxes 2 and 4 contain less clustering (Fig. 1, A and B). In considering this difference, we have noted that the boundary between box 2 and box 3 lies in the area of significant geological changes along the San Andreas fault (*6, 7*). These changes include (i) the appearance of Franciscan rocks in contact with the fault zone at the surface, which does not occur to the south; (ii) the northward merging of the Table Mountain fault and Parkfield syncline with the San Andreas fault; and (iii) the northern topographic termination of Middle Mountain, under which at least the last few moderate Parkfield earthquakes have taken place (*1, 2, 8*). To the north of this area, the San Andreas fault slips mostly by creep, whereas to the south the creep rate declines, and slip on the fault is accommodated mainly by moderate earthquakes. Thus, the clustering of microearthquakes in box 3 may be related to the geometric interaction of faults or fault segments that also juxtapose rocks of different mechanical properties north and south of this region.

We propose that the episode of increased fault slip at Parkfield resulted from a stress diffusion process that originated somewhere below the seismically active region northwest of Parkfield. This proposal stems from the observation that the changes in cumulative moment that began in 1990 first took place in the northwest and then in the southeast. A linear fit across the contours in Fig. 3B suggests that the propagation speed of this process along the San Andreas fault is 30 to 50 km/year. This disturbance may not have originated on the San Andreas fault itself because the initial increase in earthquake-related slip took place outside of this fault zone (Fig. 2).

The southeastward movement of earthquake activity at Parkfield is not without precedent. A series of $M \geq 4$ foreshocks that evidently moved southeastward toward the location of the main shocks were associated with both the 1934 and 1966 Parkfield $M > 5$ earthquakes (*1, 8, 9*). These foreshocks took place over the period of a couple of months and spanned 15 km of the fault, suggesting a stress disturbance that propagated at speeds of 60 to 100 km/year. Stress disturbances with propagation speeds even larger than these—approximately 100 to 200 km/year—have also been suggested for event sequences that have been observed in Turkey and China (*10, 11*).

We have considered our observations in the light of a mechanical model for stress diffusion along a rupturing plate boundary like that of the San Andreas fault (*12*). In the stress diffusion model, the critical parameter is the propagation speed of the type of deformation front that drives the microearthquake activity. Theoretical analysis of stress relaxation below the seismogenic zone of a rupturing boundary indicates that when the stress diffusion speeds are reduced to less than 100 to 200 km/year by overlying fault asperities (strong inhomogeneities in fault strength), the result is elastic loading of these features (*12*). In our model, the rate of this loading would be proportional to the rate of the fault's microearthquake activity and the trend of the cumulative moment. Continued monitoring of the magnitude-latitude-time character of microearthquakes might thus detect a loading event that could cause the next moderate Parkfield earthquake.

REFERENCES AND NOTES

1. W. H. Bakun and T. V. McEvilly, *Science* **205**, 1375 (1979).
2. ———, *J. Geophys. Res.* **89**, 3051 (1984).
3. W. H. Bakun and A. G. Lindh, *Science* **229**, 619 (1985).
4. P. E. Malin, S. N. Blakeslee, M. G. Alvarez, A. J. Martin, *ibid.* **244**, 557 (1989).
5. The moments used in generating Fig. 2 represent average values that were observed at no fewer than three stations. The station moment for each event was calculated by integrating the S-wave displacement and velocity spectra over frequency and by assuming that the resulting values fit a frequency-squared model of the earthquake source. Summing these moments as a function of time yields the curves in Fig. 2. For reference to this method, see D. J. Andrews [in *Earthquake Source Mechanics*, K. Aki and P. Richards, Eds., *American Geophysical Union Monograph 37* (American Geophysical Union, Washington, DC, 1986)].
6. J. D. Sims, *U.S. Geol. Surv. Misc. Field Studies Map MF-2115* (1990).
7. W. R. Dickinson, *Geol. Soc. Am. Bull.* **77**, 707 (1966).
8. T. V. McEvilly, W. H. Bakun, K. B. Casaday, *Bull. Seismol. Soc. Am.* **57**, 1221 (1967).
9. A. G. Lindh and D. M. Boore, *ibid.* **71**, 95 (1981).
10. N. Toksoz *et al.*, *Pure Appl. Geophys.* **117**, 1258 (1979).
11. C. H. Scholz, *Nature* **267**, 121 (1977).
12. F. K. Lehner, V. C. Li, J. R. Rice, *J. Geophys. Res.* **86**, 6155 (1981).

13. We thank numerous colleagues at the University of California at Berkeley and at the U.S. Geological Survey, with whom we have shared the effort of keeping the Parkfield downhole seismology project alive. We also thank an anonymous reviewer, R. Simpson, and K. Malin for suggesting major improvements to the text. This work was supported by U.S. Geologic Survey grant 14-08-0001-G1375.

23 December 1991; accepted 12 March 1992

Electron-Tunneling Pathways in Cytochrome c

Deborah S. Wuttke, Morten J. Bjerrum,*
Jay R. Winkler, Harry B. Gray†

Distant Fe^{2+}-Ru^{3+} electronic couplings have been extracted from intramolecular electron-transfer rates in Ru(histidine^X) (where X = 33, 39, 62, and 72) derivatives of cytochrome c. The couplings increase according to 62 (0.0060) < 72 (0.057) < 33 (0.097) < 39 (0.11 per wave numbers); however, this order is out of line with the histidine to heme edge-edge distances [62 (14.8) > 39 (12.3) > 33 (11.1) > 72 (8.4 angstroms)]. The rates (and the couplings) correlate with the lengths of σ-tunneling pathways comprised of covalent bonds, hydrogen bonds, and through-space jumps from the histidines to the heme group. Space jumps greatly decrease couplings: One from Pro^{71} to Met^{80} extends the σ-tunneling length of the His^{72} pathway by roughly 10 covalent-bond units.

Both theoretical (*1–11*) and experimental (*11–16*) studies have indicated that variations in distant electronic couplings could play a major role in controlling the rates of electron transfer (ET) through proteins. The most attractive theoretical formulations are ones that explicitly include the structure of the intervening polypeptide (*4–11*); of these, the Beratan, Betts, and Onuchic (BBO) coupling maps (*4*) have proved particularly useful in designing experimental systems for study. In the BBO map for cytochrome c, there are several regions on the protein surface where the calculated couplings to the heme are substantially different from those given by an exponential-decay-with-distance model (*4*). A main goal of our work on $Ru(bpy)_2(im)(His^X)^{2+}$ (bpy is 2,2′ bipyridine, im is imidazole) derivatives (*17*) of structurally engineered cytochromes c is to develop an experimentally validated coupling map for this protein. Here we report on four regions of the map (X = 33, 39, 62, and 72).

Histidines 33, 39, 62, and 72 [33 (horse heart) (*17*); 39 (*Candida krusei*) (*18*); 62 (genetically engineered $Asn^{62} \rightarrow$ His *Saccharomyces cerevisiae*) (*19*); and 72 (semisynthetic $Lys^{72} \rightarrow$ His horse heart) (*20*)] (Fig. 1) were modified by the $Ru(bpy)_2(CO_3)$-im procedure (*17*) to give $Ru(bpy)_2(im)(His^X)$-protein derivatives (*21*). Intramolecular ET

Beckman Institute, California Institute of Technology, Pasadena, CA 91125.

*Present address: Department of Chemistry, Royal Veterinary and Agricultural University, Thorvaldsensvej 40, 1871 Frederiksberg C, Denmark.
†To whom correspondence should be addressed.